A closer look into the distance dependence of vibrational energy transfer on surfaces using 2D IR spectroscopy

Fernández-Terán, Ricardo ; Hamm, Peter

Abstract: Vibrational energy transfer (VET) between two isotopologues of [Re(dcb)(CO)3Br] immobilized on a TiO2 surface is studied with the help of 2D IR spectroscopy in dependence of surface coverage. To dilute the molecules on the surface, and thereby control the intermolecular distances, two different diluents have been used: a third isotopologue of the same molecule and 4-cyanobenzoic acid. As expected, the VET rate decreases with dilution. For a quantitative investigation of the distance dependence of the VET rate, we analyze the data based on an excitonic model. This model reveals the typical 1/r6-distance dependence for a dimer of a donor and acceptor, similar to the nuclear Overhauser effect in NMR spectroscopy or Förster resonant energy transfer in electronic spectroscopy. However, VET becomes a collective phenomenon on the surface, with the existence of a network of coupled molecules and its disappearance below a percolation threshold, dominating the concentration dependence of the VET rate.

DOI: https://doi.org/10.1063/5.0025787

A Closer Look into the Distance Dependence of Vibrational Energy Transfer on Surfaces Using 2D IR Spectroscopy

Ricardo Fernández-Terán and Peter Hamm*
Department of Chemistry, University of Zurich, Winterthurerstrasse 190, Zurich, Switzerland
* *Corresponding Author:* peter.hamm@chem.uzh.ch
(Dated: January 19, 2021)

Vibrational energy transfer between two isotopologues of [Re(dcb)$(CO)_3$Br] immobilized on a TiO_2 surface is studied with the help of 2D IR spectroscopy in dependence of surface coverage. To dilute the molecules on the surface, and thereby control the intermolecular distances, two different diluents have been used: a 3rd isotopologue of the same molecule as well as 4-cyanobenzoic acid. As expected, the vibrational energy transfer rate decreases with dilution. For a quantitative investigation of the distance dependence of the vibrational energy transfer rate, we analyze the data based on an excitonic model. This model reveals the typical $1/r^6$-distance dependence for a dimer of donor and acceptor, similar to the NOE in NMR spectroscopy or FRET in electronic spectroscopy. However, VET becomes a collective phenomenon on the surface, with the existence of a network of coupled molecules, and its disappearance below a percolation threshold, dominating the concentration dependence of the vibrational energy transfer rate.

I. INTRODUCTION

Energy transfer is a central phenomenon in nature. In photosynthetic organisms, for example, electronic energy is transferred quickly from the antenna complex to the reaction centres in femto- to picoseconds.[1] The kinetics of excitation and energy transfer in different spectral domains have been the subject of rigorous and extensive research in the past. In particular, the verification of the theoretically expected distance dependence of excitation and energy transfer rates has been experimentally achieved in two main cases: Förster resonant energy transfer (FRET),[2] and the transfer of nuclear spin polarisation between adjacent protons (nuclear Overhauser effect, NOE).[3,4] In both cases, the donor-acceptor distances were known with precision. Nowadays, FRET and NOE are routinely used as molecular rulers in the nm to Å range, finding applications in different fields across biology, biochemistry, biophysics and structural chemistry.

Intermolecular vibrational energy transfer (VET), on the other hand, has only been studied in more detail in the past decade. Previous works by Zheng and coworkers used VET and anisotropy as key elements to obtain dynamic and structural information of ion clustering in aqueous SCN^- solutions and isotope-mixed crystals.[5–12] In their work, mixtures of SCN^- and its isotopologues were used as probes for intermolecular VET and clustering, and were studied using two-dimensional infrared (2D-IR) and pump-probe spectroscopy. Our group has also recently reported on ultrafast vibrational energy transfer between isotope-labelled metal carbonyl complexes co-adsorbed on surfaces, measured by 2D IR spectroscopy.[13–15]

In Ref. 11, a model has been proposed, which assumes the coupling between neighboring chromophores to be constant in time (different from NOE in NMR spectroscopy), but the site energies of individual chromophores to fluctuate in time, e.g., due to solvent interactions. In this scenario, the VET rate between pairwise two chromophores becomes:[11]

$$k = \frac{2}{1+\exp\left(-\frac{\hbar\Delta\omega}{k_B T}\right)}\left[\frac{V^2\,\tau^{-1}}{(\Delta\omega)^2+4V^2+\tau^{-2}}\right], \qquad (1)$$

where $\Delta\omega = \omega_D - \omega_A$ is the donor-acceptor frequency difference, τ^{-1} a dephasing correlation time, and V is the transition dipole coupling between donor and acceptor modes, given by:

$$V = \kappa\frac{\mu_D\mu_A}{4\pi\varepsilon_0}\frac{1}{r^3}. \qquad (2)$$

Here, r is the donor-acceptor distance, κ is an orientational factor, $\mu_{D,A}$ the transition dipole moments of donor or acceptor, respectively, and ε_0 the vacuum permittivity. The physical picture behind this model is the following: Due to the coupling V, excitation energy is initially transferred from the donor to the acceptor in a coherent sense, as described by the time-propagation of the time-dependent Schrödinger equation. The coherence between donor and acceptor state is then abruptly terminated by a random and dephasing event after an average time τ,[11] revealing a first-order kinetics with rate described by Eq. 1. In the weak coupling limit $V \ll \Delta\omega$, which is assumed anyways in the derivation of Eq. 1, the VET rate scales with the characteristic $1/r^6$ dependence (Eqs. 1 together with 2), as in FRET and NOESY, despite the fact that the mechanisms are slightly different in these cases.

Immobilisation of molecular catalysts on surfaces constitutes a promising strategy towards the construction of a functional artificial photosynthetic system, akin to nature's own approach.[16] It has been shown that some CO_2 reduction catalysts like Re(I) tricarbonyls can be adsorbed on a metal oxide surface while retaining their catalytic activity.[16–21] In addition, the electron transfer steps potentially involved in photocatalytic proton

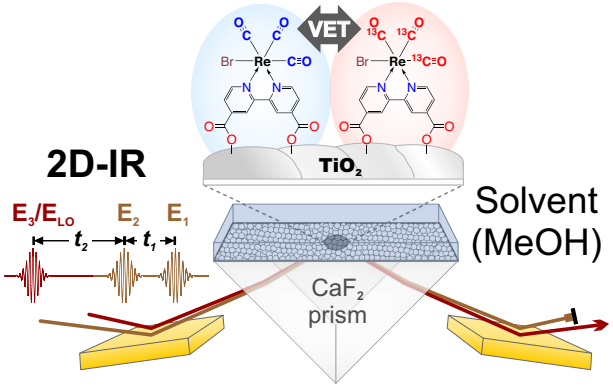

FIG. 1. Experimental scheme of 2D IR spectroscopy to observe ultrafast vibrational energy transfer (VET) on a TiO_2 surface.

or CO_2 reduction have been studied on hybrid materials consisting of a Re(I) tricarbonyl photosensitiser and/or catalyst, (co-)adsorbed on a metal oxide surface.[18,22–25]

Due to the very steep $1/r^6$ dependence of the coupling on the donor-acceptor separation, VET can only be observed between molecules situated at very close proximity. Immobilisation on a surface thus poses the ideal scenario for studying vibrational energy transfer. Apart from the drastic reduction in intermolecular distances, the *static* character of the anchoring removes diffusion from the overall picture, simplifying its further analysis and removing any potential time-dependence of the donor-acceptor distance.

The stretching vibrations of transition metal carbonyl complexes have one of the highest transition dipoles (large $\vec{\mu}$) and relatively long vibrational lifetimes (in the order of 10–100 ps), making them the ideal chromophores to understand vibrational energy transfer in detail. With this in mind, we set to examine more closely the variables that affect vibrational energy transfer on heterogeneous surfaces. To that end, we used a mixture of co-adsorbed isotopologues of a Re(I) tricarbonyl complex, [Re(dcb)$(CO)_3$Br] (dcb = 2,2'-bipyridine-4,4'-dicarboxylic acid), as the framework to understand catalyst-catalyst interactions on the surface (Fig. 1). Furthermore, we also performed a dilution with a different molecule (4-cyanobenzoic acid, **CNBz**), which served as a model system for the study of the interaction between two molecules of different sizes.

II. EXPERIMENTAL METHODS

A. Synthesis and Characterization of the Complexes

All chemicals and solvents for the synthesis were of reagent grade, and were used without further purification. $[Re(CO)_3Br_3]^{2-}$ was synthesized according to previously reported procedures.[26] The unlabelled complex, [Re(dcb)$(CO)_3$Br], **Re(^{12}CO)**, was prepared from $Re^{I}(CO)_5Br$ (Sigma-Aldrich) following a previously reported procedure.[27]

The CO isotope-labelled complexes, **Re(^{13}C^{16}O)** and **Re(^{13}C^{18}O)**, were prepared in two steps. First, a DMF solution of $[Re(CO)_3Br_3][N(Et)_4]_2$ (20 mM) was bubbled with the corresponding isotope-labelled CO gas (99% ^{13}C; or 99% ^{13}C, 95% ^{18}O, resp.; Sigma-Aldrich), for about a month at room temperature in a septum-sealed round bottom flask. Isotopic conversion of the starting material into the fully-labelled $[Re(*CO)_4Br_2]^-$ complex (where *CO refers to $^{13}C^{16}O$ or $^{13}C^{18}O$, respectively) was monitored by FT-IR spectroscopy (Figs. S1 and S2 in the Supporting Information). In a subsequent step, after removal of the solvents, the labelled $[Re(*CO)_4Br_2]^-$ precursor was dissolved in MeOH/Toluene (2:3 volume ratio, [Re] ≈ 5 mM), and after addition of the dcb ligand (1 equiv.), the solution was refluxed for 5 h, filtered while hot through a thin glass frit, and the solvents were evaporated under reduced pressure. After drying under high vacuum, the complexes were obtained as orange-reddish solids in excellent yields (>80%) and isotopic purities (>90%), as verified by FT-IR spectroscopy.

B. Sample Preparation

For the preparation of the samples for 2D IR spectroscopy, we followed a similar approach as previously reported in Ref. 15. In brief, the reflective plane of a 1 cm CaF_2 right-angle prism (Thorlabs) was coated with a 30 nm thick ALD-deposited TiO_2 layer, after which a suspension of rutile TiO_2 nanoparticles (50 nm diameter) was spin-coated (thickness ≈ 0.5 μm). The prisms were annealed at 550 °C for 1 h, then soaked for one week at room temperature in the corresponding MeOH solutions containing a 1:1 mixture of **Re(^{12}C^{16}O)** and **Re(^{13}C^{16}O)**, and the diluent in different concentrations. As diluents, we used **Re(^{13}C^{18}O)** or 4-cyanobenzoic acid (**CNBz**). The total Re(I) concentration was fixed at 0.2 mM for dilution with **Re(^{13}C^{18}O)**, and was decreased proportionally when diluting with **CNBz**. Quantification of the adsorption ratio of **CNBz** vs **ReCO** is described in the Supporting Information.

C. Ultrafast 2D IR Spectroscopy

The ultrafast 2D IR spectrometer used in this work constitutes a slight modification of our previously reported setup.[28] In brief, the output of a 5 kHz Ti:Sapphire amplifier producing ≈100 fs pulses centered at 800 nm, was used to pump a home-built mid-IR OPA,[29,30] delivering ≈2 μJ, ca. 120 fs pulses centred around 2000 cm^{-1}. A small fraction of the mid-IR light was split from a BaF_2 wedge to be used as the probe and reference beams. Absorptive 2D IR spectra were obtained by fast scanning the coherence delay between the

two mid-IR pump pulses (up to 5 ps, revealing a ω_1 resolution of $\approx$2 cm^{-1} after zero-padding) generated in a Mach-Zehnder interferometer for a fixed population delay (t_2). The spectral distribution of the pump pulse was accounted for by dividing the 2D-IR spectra across ω_1 by the pump spectrum (obtained from the pump interferogram) prior to analysis.[31] Scattering suppression was achieved by quasi-phase cycling using a librating ZnSe window introduced in the pump beam at Brewster angle.[32] The pump and probe beams were overlapped at the sample position, and afterwards the probe and reference beams were dispersed in a spectrograph with a 150 l mm^{-1} grating, and simultaneously recorded with a 2×32 pixels MCT detector, yielding a ω_3 resolution of $\approx$5 cm^{-1}.

All data have been measured in the ATR geometry shown in Fig. 1, with pump and probe beams *s*-polarized respect to the prism surface. With the exception of the surface data shown in Fig. 3 below (blue line), the prism surface was immersed in MeOH in all other experiments. These surface data were measured in an FTIR spectrometer instead of the laser system, whose larger beam size was incompatible with the very shallow ATR angle of CaF_2 vs MeOH, and permitted measurements against air only.

D. 2D-IR Data Analysis

Special attention must be put to a subtle but important detail concerning the normalisation of the different kinetic traces, and is discussed in the following. As has been described previously, it is the volume of the peak rather than its intensity that is preserved, even in the presence of spectral diffusion.[33] In the present work, the peak volumes were extracted by fitting to a correlated two-dimensional Gaussian function of the form:[34]

$$G(\omega_1,\omega_3) = A\exp\Bigg\{-\frac{1}{2(1-c^2)}\Bigg[\left(\frac{\omega_1-\omega_{1,0}}{\sigma_{\omega_1}}\right)^2 + \left(\frac{\omega_3-\omega_{3,0}}{\sigma_{\omega_3}}\right)^2 - \frac{2c(\omega_1-\omega_{1,0})(\omega_3-\omega_{3,0})}{\sigma_{\omega_1}\sigma_{\omega_3}}\Bigg]\Bigg\}, \tag{3}$$

where A is an amplitude, c is a correlation coefficient as a measure of spectral diffusion,[34] $\omega_{x,0}$ refers to the centre frequencies along each axis, and σ_{ω_x} refers to the width of the projection of the Gaussian along each axis (related to the homogeneous and inhomogeneous line widths). The volumes of the fitted peaks (Φ) were calculated from the obtained parameters using the following relationship:

$$\Phi = 2\pi A\sigma_{\omega_1}\sigma_{\omega_3}\sqrt{1-c^2}. \tag{4}$$

The intensity of a 2D IR cross peak scales with $\|\vec{\mu}_{\rm pu}\|^2\|\vec{\mu}_{\rm pr}\|^2$, where pu and pr stand for the pumped and probed oscillators, respectively. With this in mind, the energy transfer kinetics can then be retrieved by normalising the cross peak volumes by $\sqrt{\Phi_{\rm pu}\Phi_{\rm pr}}$, where $\Phi_{\rm pu}$ and $\Phi_{\rm pr}$, respectively, are the volumes of the corresponding diagonal peaks at time zero. This procedure was performed under identical conditions for both experimental and simulated spectra.

III. SIMULATION METHODS

A. Exciton Hamiltonian

In this work, we employ the exciton Hamiltonian for N oscillators:[35,36]

$$H(t) = \sum_{i=1}^{N}\left[\omega_i(t)b_i^\dagger b_i - \frac{\Delta_i}{2}b_i^\dagger b_i^\dagger b_i b_i\right] + \sum_{i,j}^{N}\beta_{ij}b_i^\dagger b_i + \sum_{i=1}^{N}\vec{\mu_i}\cdot\vec{E}(t)\left[b_i^\dagger + b_i\right], \tag{5}$$

where $b_i^\dagger$ and b_i the harmonic creation and annihilation operators, ω_i the frequencies of mode i and Δ_i their anharmonicities. The coupling β_{ij} between modes i and j is given by:

$$\beta_{ij} = \frac{1}{4\pi\varepsilon_0}\left[\frac{\vec{\mu}_i\cdot\vec{\mu}_j}{r_{ij}^3} - 3\frac{(\vec{r}_{ij}\cdot\vec{\mu}_i)(\vec{r}_{ij}\cdot\vec{\mu}_j)}{r_{ij}^5}\right], \tag{6}$$

where $\vec{r}_{ij}$ is the vector connecting sites i and j. The interaction of vibrational modes with an applied external mid-IR field $\vec{E}(t)$ takes place through the transition dipoles $\vec{\mu}_i$. Due to surface anchoring, we assumed in our model that the transition dipoles as well as the intermolecular distances are static, leading to time-independent β_{ij}. Time-dependent fundamental frequencies were obtained for mode i from:

$$\omega_i(t_k) = \omega_0 + \delta\omega_{i,inhom}(t_k) + \delta\omega_{i,hom}(t_k), \tag{7}$$

with an δ-correlated homogeneous contribution:

$$\delta\omega_{i,hom}(t_k) = \Omega_{hom}\mathcal{N}(0,1) \tag{8}$$

as well as a spectral diffusion process:

$$\delta\omega_{i,inhom}(t_k) = e^{-\Delta t/\tau_c}\delta\omega_{i,inhom}(t_{k-1}) + \sqrt{1-e^{-2\Delta t/\tau_c}}\Omega_{\rm inhom}\mathcal{N}(0,1). \tag{9}$$

In these equations, ω_0 is the mean frequency of the mode (which varies with isotope substitution), $\Delta t = t_{i+1} - t_i$ is the time step of the simulation (200 fs), over which the frequency is assumed to be constant, $\Omega_{\rm hom}$ and $\Omega_{\rm inhom}$ the width of the homogeneous and inhomogeneous contributions, respectively, and $\mathcal{N}(0,1)$ random numbers from a normal distribution with zero mean and unit variance that are drawn independently at each time point and for each oscillator. $\Omega_{\rm hom}$ is related to the homogeneous dephasing time T_2 by $\Omega_{\rm hom} = 1/\sqrt{T_2\Delta t}$,[36] while Eq. 9

reveals a Gaussian process whose autocorrelation function decays exponentially with time constant τ_c,[37] and models spectral diffusion.

Based on this Hamiltonian, 2D IR spectra were calculated by formulating the in total 6 response functions of ground state bleach (GB), stimulated emission (SE) and excited state absorption (EA) in the the two phase matching directions that contribute to purely absorptive 2D IR spectra, see Eq. 15 of Ref. 38. For the calculation of the time-evolution matrices needed in that scheme, however, a somewhat different approach than in Ref. 38 was taken, which is discussed in Appendix A. If not noted otherwise, all response functions where multiplied with an exponential decay with time constant of 20 ps, accounting for T_1 relaxation in a phenomenological manner. For a donor-acceptor dimer, the excitonic model reproduces Eq. 1, as also discussed in the Appendix A.

B. Simulation Parameters

To simulate 1D and 2D IR spectra of the a'(1) ν_{CO} band of the Re(I) tricarbonyl complexes on the surface, the following parameters were used: transition dipole $\mu = 0.35$ D,[13] anharmonicity $\Delta_{CO} = 5$ cm^{-1}, dephasing time (T_2) of 1.5 ps, inhomogeneous width $\Omega_{inhom} = 4.2$ cm^{-1}, and spectral diffusion correlation time $\tau_c = 20$ ps. The line shape parameters have been optimised to match experimental 1D and 2D IR spectra (see below). The oscillators were placed on a flat surface, and elevation angles in the range $20° \leq \theta \leq 35°$ were considered, based on previous reports about the molecular orientations of similar complexes on TiO_2 by Lian and co-workers, as well as Petersen and co-workers.[39–42]

For simulations of the saturated surface and dilution with **Re(**^{13}**C**^{18}**O)**, 49 molecules were placed on a 43.5×43.5 Å box with periodic boundary conditions (PBC), and randomised with short pseudo-MD runs simulating the chromophores as Lennard-Jones liquid. We stress that this pseudo-MD runs are not aimed to be atomistic simulations; their purpose is to generate randomised molecular arrangements on the (idealized) surface that are characterized by a radial distribution function (RDF). The Lennard-Jones diameter used for these simulations (5.7 Å) has been adjusted to reveal the experimental coupling strength (see below).

A typical snapshot of a 1:1 distribution of the two isotopologues on the surface calculated in this way is shown in Fig. 2A, and in Fig. 2B, black, the corresponding radial distribution function (RDF). Integrating over the first peak of the RDF up to the fist minimum, we obtain a coordination number of 5.8, in close agreement with the expected 6 nearest neighbours for a closest packing.

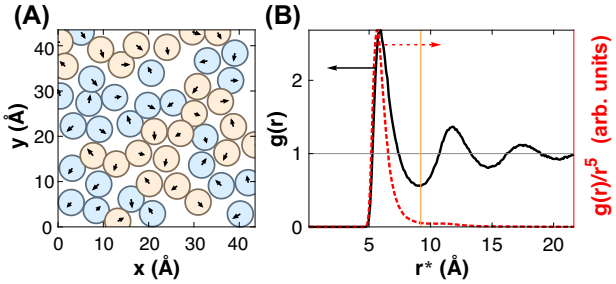

FIG. 2. (A) Typical snapshot of a simulated distribution of chromophores on the surface. The arrows are proportional to the projection of $\vec{\mu}$ on the xy-plane. The ^{12}C^{16}O and ^{13}C^{16}O isotopologues are coloured in blue and orange, respectively. (B) RDF $g(r)$ in black and $g(r)/r^5$ in red. The orange vertical line marks the extent of the first coordination shell.

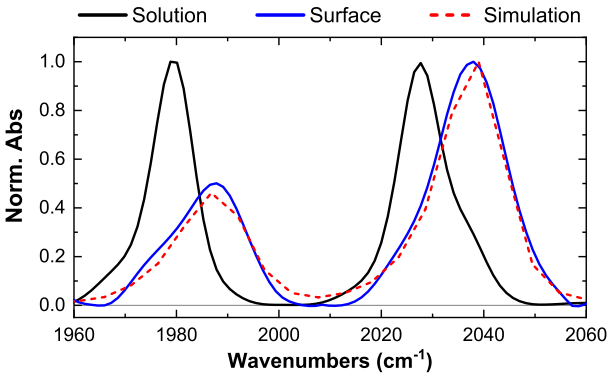

FIG. 3. Normalised IR absorption spectra of a 1:1 isotopic mixture of **Re(**^{12}**C**^{16}**O)** and **Re(**^{13}**C**^{16}**O)**, comparing the soaking solution in MeOH (solid black line) with that after immobilising the molecules on the surface (solid blue line, as dry film, see Experimental Methods for details). Also shown is the corresponding simulated spectrum (dashed red line).

IV. NO DILUTION: CLOSE-TO-CLOSEST PACKING ON THE SURFACE

A. 1D Spectra

As a starting point, we compare in Fig. 3 the experimental 1D spectra (solid blue line) in the region of the of the a'(1) carbonyl stretching modes of a 1:1 **Re(**^{12}**C**^{16}**O)**:**Re(**^{13}**C**^{16}**O)** isotopic mixtures on the surface with that of the original MeOH soaking solution (solid black line) used to prepare the films. Upon immobilisation, both bands experience a blue shift of 10 cm^{-1} and become slightly broader. The most striking difference, however, comes from their intensity ratios. The initial 1:1 intensity ratio in the soaking solution decreases to approximately 0.5:1 upon adsorption on the surface, with the band of the ^{13}C^{16}O isotopologue becoming less intense in proportion. Both isotopologues are chemically identical and we can safely assume that their ratio is still 1:1 on the surface. As discussed previously by

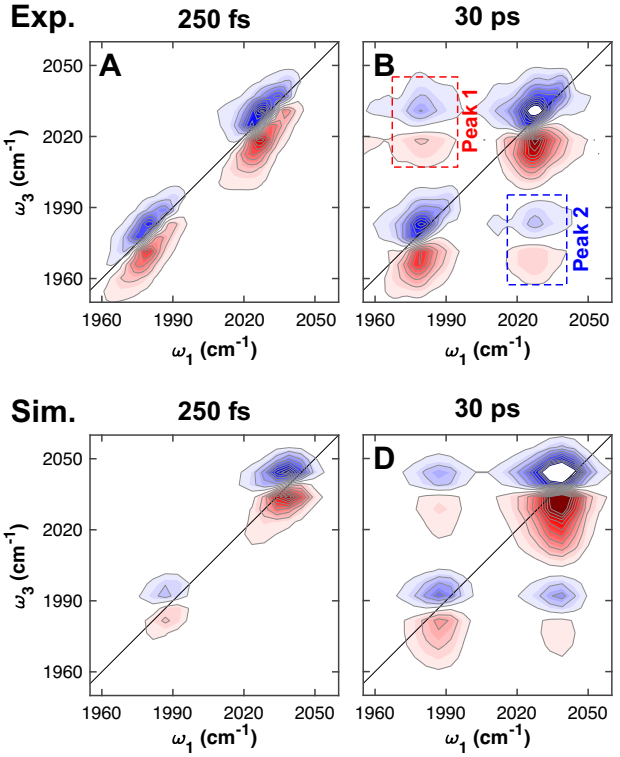

FIG. 4. Experimental (A-B) and simulated (C-D) 2D IR spectra of a saturated surface with 1:1 $\mathbf{Re(^{12}C^{16}O)}$:$\mathbf{Re(^{13}C^{16}O)}$ (immersed in MeOH) at 1 and 30 ps. Peaks 1 and 2 refer to the uphill and downhill VET cross-peaks, respectively. The scale of panels B,D has been increased to 50% of the maximum to emphasize the weak cross peak.

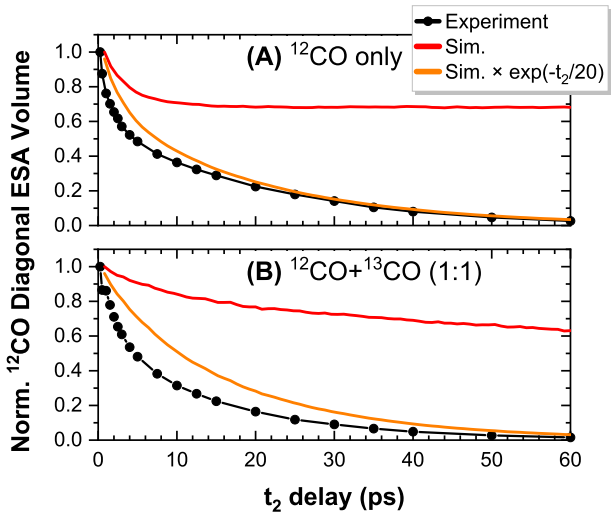

FIG. 5. Kinetics of the diagonal peaks of the $^{12}C^{16}O$ a'(1) band of (A) a sample containing only $\mathbf{Re(^{12}C^{16}O)}$ and (B) a 1:1 mixture of $\mathbf{Re(^{13}C^{16}O)}$ and $\mathbf{Re(^{12}C^{16}O)}$. In either case, the experimental data are shown in black, simulation results in red, and simulation results multiplied with an exponential decay with time constant of 20 ps, representing T_1 relaxation in orange.

Zanni and co-workers,[43] the transition dipole strength is the most sensitive indicator of coupling between vibrational modes. While frequency shifts are also observed upon intermode coupling, these are typically well below the line width of most condensed-phase modes (typically 10 cm^{-1}), and furthermore may be masked by solvent effects. We attribute the redistribution of oscillator strength between the bands of the two isotopologues to vibrational coupling. In fact, we adjusted the Lennard-Jones diameter in the pseudo-MD simulation (in a trial-and-error procedure) to reproduce the experimental intensity ratio (Fig. 3, dashed red line), revealing typical couplings in the range of $V \approx 3$–5 cm^{-1} between nearest neighbours.

B. 2D Spectra: Diagonal Peak Dynamics

Fig. 4 exemplifies experimental and simulated 2D IR spectra at early (250 fs) and late (30 ps) population times. At early populations times, only diagonal peaks are visible, which are tilted along the diagonal due to an inhomogeneous distribution of oscillator frequencies. At later populations times, that tilt largely disappears due to spectral diffusion. The line-shape parameters, which went into Eqs. 5-9 (Δ, ω_0, T_2, Ω_{inhom} and τ_c), were adjusted to best match the shape and dynamics of these diagonal peaks.

In a first step, we focus on the volume of the diagonal peaks. In agreement with our previous report,[13] the experimentally observed diagonal peaks decay in a biexponential manner, with time constants and amplitudes of 2.6 ps (≈40%) and 16 ps (≈60%), respectively, for the 1:1 mixture of $\mathbf{Re(^{12}C^{16}O)}$:$\mathbf{Re(^{13}C^{16}O)}$ (Fig. 5B, black). Also for a pure $\mathbf{Re(^{12}C^{16}O)}$ sample, we observe 1.1 ps (≈40%) and 19 ps (≈60%, see Fig. 5A, black). Such biexponential decays have been observed in similar Re(I)-tricarbonyl complexes both adsorbed on surfaces,[44,45] and to a lesser extent also in solution.[46] The faster component in this biexponential decay has been explained by orientational relaxation[45] and/or intramolecular vibrational energy redistribution (IVR) to the other CO stretching modes of the molecule,[13,44,46] while the slower component was attributed to population relaxation (T_1) to lower frequency modes.

However, contradicting results have been obtained in solution, observing biexponential[46] or mono-exponential decay kinetics,[47] which questions the explanations given in Refs. 13, 44, and 45 for the biexponential decay on the surface, since these explanations all are of intramolecular nature and as such should apply in the same way on the surface and in solution. Here we offer an alternative explanation for the biexponential kinetics observed on the surface. Fig. 5A, red, shows the result of a simulation with only one isotopologue on the surface as the easiest possible situation, without including T_1 relaxation and IVR to the other CO modes (both of which are not part of

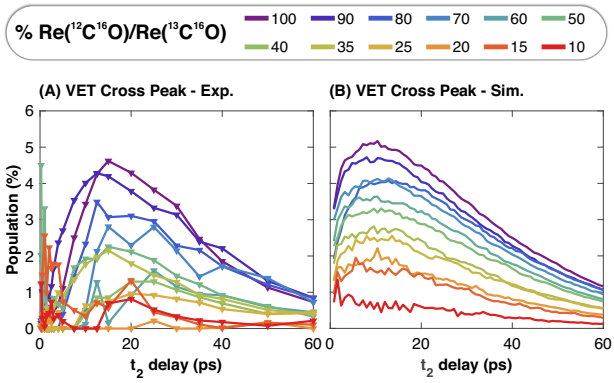

FIG. 6. Experimental (A) and simulated (B) cross peak kinetics of the downhill VET between the a'(1) CO stretches (peak 2) as a function of concentration of $\mathbf{Re(^{12}C^{16}O)/Re(^{13}C^{16}O)}$ relative to $\mathbf{Re(^{13}C^{18}O)}$. Experiments were performed with the surface immersed in MeOH.

the excitonic model), and without the possibility of VET to another isotopologue. An initial decay with time constant 3.3 ps is followed by a constant pedestal in this case. When multiplying these data with an an exponential decay with time constant of 20 ps, representing T_1 relaxation in a phenomenological manner (Fig. 5A, orange), a biexponential decay is obtained, in close agreement with experiment (Fig. 5A, black). The same simulations of an 1:1 mixture of two isotopologues (Fig. 5B, red) reveal a biexponential decay (8.5 ps, 20%, and 240 ps, 80%), even before adding T_1 relaxation.

We have seen in Sec. IV A that the coupling on the surface is strong enough to redistribute oscillator strength between excitonic states. Those with higher oscillator strength will be excited preferentially by the pump pulses in the 2D IR experiment. As a result of VET, excitation energy will subsequently be scattered into the lower-energy excitonic states, thereby reducing intensity of the diagonal peaks in the 2D IR spectra. The energy spacing $\Delta\omega$ enters in the VET rate (Eq. 1). If only one isotopologue is present, $\Delta\omega$ is small and VET is fast (Fig. 5A, red). With two isotopologues on the surface, two different $\Delta\omega$'s become relevant – within each isotopologue and between the two isotopologues– revealing two different timescales for the decay of the diagonal peak intensity (Fig. 5B, red).

C. 2D Spectra: Cross Peak Dynamics

Returning to Fig. 4, we now discuss the cross-peaks. At early delay times, no cross peaks are visible on the scale of Fig. 4. The coupling discussed in Sec. IV A is too weak to reveal instantaneous cross peaks, whose intensities scale as $(2V/\Delta\omega)^2 \approx 4\%$.[36] However, cross peaks grow in as a function of population time resulting from VET, see Fig. 4 B,D. Peak 1 corresponds to the VET from $\mathbf{Re(^{13}C^{16}O)}$ to $\mathbf{Re(^{12}C^{16}O)}$ (uphill transfer), while peak 2 corresponds to the transfer from $\mathbf{Re(^{12}C^{16}O)}$ to $\mathbf{Re(^{13}C^{16}O)}$ (downhill transfer). The violet lines in Fig. 6A (i.e., for 100% $\mathbf{Re(^{12}C^{16}O)/Re(^{13}C^{16}O)}$) show the populations represented by these cross peaks as a function of time. To that end, we evaluated the volume of the ESA cross peak of peak 2 (downhill VET), which is better separated, and thus less affected by the stronger diagonal peaks. The cross peak volume initially rises due to VET, peaks at about 15 ps, and then decays due to overall population relaxation. These results are in essence the same as those reported earlier,[13] where we have modelled the data as a phenomenological rate-equation scheme with exchange due to VET with time constants of 90 and 70 ps, respectively, for the uphill and the downhill VET, as well as bi-exponential population (T_1) relaxation with 3 ps and 20 ps time constants. Since VET is slower than T_1 relaxation, the maximum of the cross peak population remains low (around 5%). Simulating this process with the excitonic model, with parameters that have been pre-determined from the diagonal peaks as discussed above, can reproduce the experimental results almost quantitatively (Fig. 6B, violet), both in terms of the position and the height of the peak of the signal.

V. SURFACE DILUTION WITH A BIG MOLECULE

Next, we discuss a series of measurements with of a 1:1 mixture of $\mathbf{Re(^{12}C^{16}O)/Re(^{13}C^{16}O)}$ diluted by a 3rd isotopologue, $\mathbf{Re(^{13}C^{18}O)}$, co-adsorbed on the surface. All three molecules are chemically identical, hence the distribution of molecules on the surface will be purely statistical and reflect that of the soaking solution. The kinetics of the VET cross peak between $\mathbf{Re(^{12}C^{16}O)}$ and $\mathbf{Re(^{13}C^{16}O)}$ (Fig. 6A) as a function of the relative concentration of $\mathbf{Re(^{13}C^{18}O)}$ reveal a decay in amplitude upon dilution, as expected. The simulations reveal an excellent agreement with the experiment in terms of the change in amplitude and kinetic behaviour of the cross peaks (Fig. 6B). In these simulations, we used the same spatial distribution of chomophores as before (Fig. 2A), but now randomly assigned the three isotopologues with the corresponding probability. The excitonic model does include the VET pathways from either $\mathbf{Re(^{12}C^{16}O)}$ or $\mathbf{Re(^{13}C^{16}O)}$ to $\mathbf{Re(^{13}C^{18}O)}$, which is happening both in experiment and simulation, but are not shown here.

Interestingly, apart from an amplitude change, the cross peak kinetics do not seem to change a lot upon $\mathbf{Re(^{13}C^{18}O)}$ dilution, despite the fact that new relaxation pathways open up. Since T_1 relaxation is significantly faster than cross relaxation, is masks most of the cross peak kinetics at later times, which would become more complex if more than two states were involved. However, regardless of how complicated the kinetics would be at later times, the initial slope of the cross-peak volume reflects directly the rate constant be-

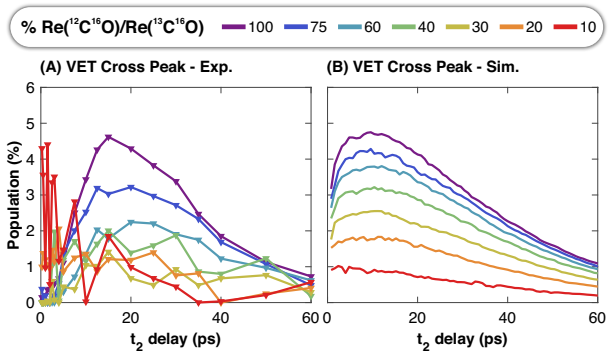

FIG. 7. Experimental (A) and simulated (B) cross peak kinetics of the downhill VET as a function of the concentration of **Re(^{12}C^{16}O)/Re(^{13}C^{16}O)** relative to **CNBz**. Experiments were performed with the surface immersed in MeOH.

tween the two corresponding states. Since the maximum cross population remains low in all cases ($\lesssim$5%, owing to the fast T_1 relaxation), it is –to a very good approximation– only that initial slope in combination with the T_1 relaxation rate that determines the cross peak response. As the initial slope gets smaller with **Re(^{13}C^{18}O)** dilution, the peak amplitude gets smaller. For the same reason, kinetic pathways to the two other CO modes of the **Re(CO)** complex (which exist as well) do also not complicate the analysis.

The red plot in Fig. 2B shows the weighted radial distribution function $g(r)/r^5$. This weighting considers the expected r^{-6}-dependence of the VET rate (Eqs. 1 together with 2) and the fact that the radial distribution function in 2D already contains one $1/r$ factor, which accounts for the linear scaling of the number of possible acceptor molecules with r. One can see that VET is in essence only possible to molecules in the first coordination shell. Dilution with **Re(^{13}C^{18}O)** will effectively replace these nearest neighbours in a statistical manner, reducing the overall probability for the transfer. Below 15% **Re(^{12}C^{16}O)/Re(^{13}C^{16}O)** concentration, statistically all nearest neighbours are replaced by a **Re(^{13}C^{18}O)** molecule and no VET can be observed anymore between the **Re(^{12}C^{16}O)** and **Re(^{13}C^{16}O)** isotopologues.

VI. SURFACE DILUTION WITH A SMALL MOLECULE

In order to avoid the complication of VET to the diluent **Re(^{13}C^{18}O)**, and to vary intermolecular distances in smaller steps, we introduce in the following a set of experiments, where 4-cyanobenzoic acid (**CNBz**) was used as the surface diluent instead. Despite the fact that these molecules are now chemically different, the ratio on the surface closely resembles that of the soaking solution, as verified by HPLC (see Supporting Information for details). The kinetics of the downhill VET cross peak as

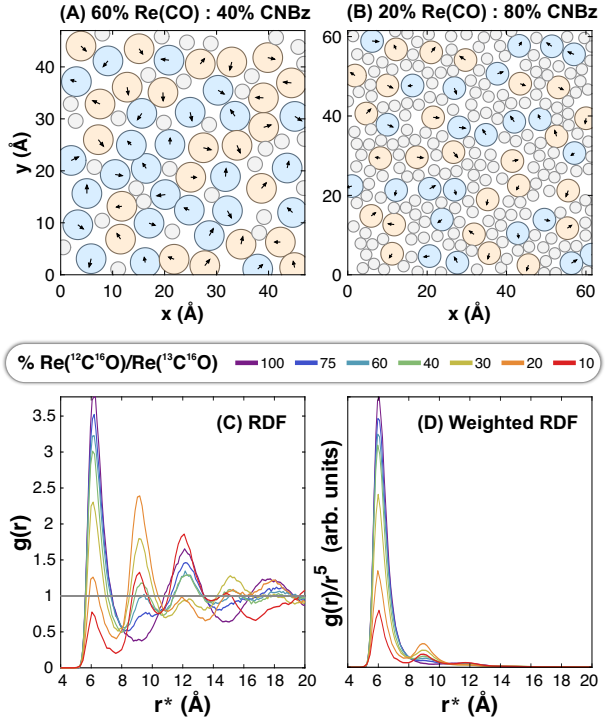

FIG. 8. Simulated surface snapshots for (A) 60% and (B) 20% **Re(CO)** concentration. Panel (C) shows the RDF in dependence of the **Re(CO)** concentration and panel (D) the corresponding weighted RDFs $g(r)/r^5$.

a function of the relative concentration of **Re(CO)** on the surface are shown in Fig. 7A. Akin to the results discussed in the previous section, the amplitudes of the cross peaks decrease upon dilution with **CNBz**, until it is no longer observable below ca. 20% **Re(CO)** concentration.

A similar procedure was followed as before for the simulations, with the Lennard-Jones diameter of the **CNBz** molecules taken as 2.35 Å—half of that of the **Re(CO)** complexes, based on the experimental crystal structures for both molecules.[48] Dilution was simulated in this case by keeping the number of **Re(CO)** molecules constant and adding additional **CNBz** molecules to the simulation box. The box size was increased accordingly so that the fraction of total area occupied by **Re(CO)** and **CNBz** was kept constant. Fig. 7B shows the simulated cross-peak dynamics, which again agree very nicely with experiment.

To analyze these results in more detail, we start with the distribution of molecules on the surface shown in Fig. 8A,B. **CNBz** molecules intercalate between the **Re(CO)** molecules, increasing the intermolecular distance by an amount roughly equal to the size of **CNBz**. This process results in a new peak showing up in the RDF of **Re(CO)** at around 8.6 Å (Fig. 8C), the sum of the two Lennard-Jones diameters. For that second peak, the VET rate is expected to go down by a factor $(5.9/8.6)^5 \approx 1/8$, based on Eq. 1. The weighted RDF shown in Fig. 8D suggests that this second peak should

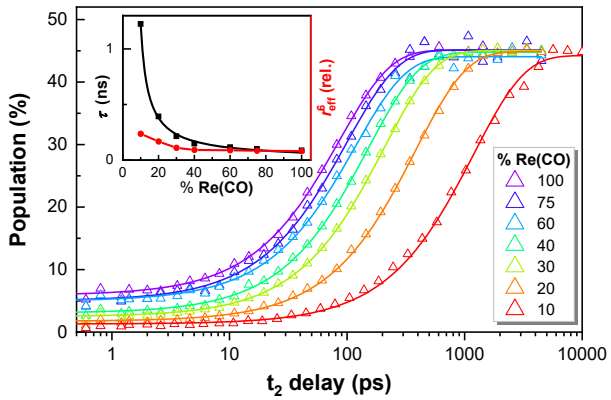

FIG. 9. VET kinetics without inclusion of T_1 relaxation for various concentrations of **Re(CO)**. Mono-exponential fist are shown. The inset plots the time-constant of these mono-exponential fits as a function of **Re(CO)** concentration together with a fit according to Eq. 10 (black), as well as r_{eff}^6 defined in Eq. 11 (red).

contribute to VET to a sizeably extent at lower **Re(CO)** concentrations.

In Fig. 9, we explore how this bimodal weighted RDF affects the VET kinetics; one might assume bi-exponential kinetics. To that end, we simulated the VET kinetics to very long times (up to 10 ns) until full equilibration is reached and show them in Fig. 9 without inclusion of T_1 relaxation; an "experiment" we cannot do in real but we can do in computer simulations. While the kinetics slow down upon dilution as expected, they remain very close to mono-exponential at all dilution factors. In light of the very heterogeneous local environments around a given **Re(CO)** molecule with a bimodal distribution of intermolecular distances (Fig. 8D), the mono-exponential character of the VET kinetics is surprising. We explain this result by the fact that the initial CO excitations are delocalized over a certain number of **Re(CO)** molecules, as evidenced by the redistribution of oscillator strength between the CO modes of the two isotopologues (Fig. 3). Consequently, VET averages over many such local environments and becomes more homogeneous.

The inset of Fig. 9 (black squares) further supports this conclusion. We see that the time-constants of the mono-exponential fits diverge at a critical concentration p_c that is larger than zero. In fact, the time constants can be fit to a function:

$$\tau(p) = \frac{\tau_0}{(p - p_c)^\alpha} \tag{10}$$

with p_c=6.3%, τ_0=64 ps and $\alpha = 0.9$ (Fig. 9, black line). Such a dependence is typical for critical phenomena, as they do occur for a percolation transition.[49] At concentrations larger than p_c, there is a connected network of coupled **Re(CO)** molecules and the vibrational excitations are delocalized over that network. Below p_c, that network fragments into small patches, and VET dies out.

The concentration dependence is steeper than what would be expected from a r^6-dependence (Fig. 9, inset, black vs red). When for example defining an effective distance as:

$$r_{eff} = \frac{\int_0^\infty r g(r)/r^5 dr}{\int_0^\infty g(r)/r^5 dr}, \tag{11}$$

it increases only by a factor 1.20 when going from 100% to 10% **Re(CO)** concentration, from which one would estimate a slowdown of VET by a factor ≈3 if an r_{eff}^6-dependence would apply, while the observed slow-down is by a factor ≈ 14. VET on the surface is a collective phenomenon that is not described properly by Eq. 1, the latter of which is valid only for a dimer.

VII. CONCLUDING REMARKS

We studied VET on a surface in dependence of surface coverage, diluting the active molecules in two different ways, i.e. by either adding another isotopologue or by adding a different, smaller molecule. In contrast to our previous works,[13] where we had fitted the data with a phenomenological rate equation model, we now use an excitonic model with explicit time-propagation of the Hamiltonian to model the experimental data. Since molecules are immobilized on the surface, only the diagonal elements of the Hamiltonian are time-dependent, presumably due to solvent fluctuations, while the off-diagonal couplings, reflecting the morphology of molecules on the surface, were assumed to be static. Loosely speaking, the diagonal elements of the Hamiltonian are represented by the diagonal peaks in the 2D IR spectra, and in fact the Hamiltonian was parametrized only based on the the shape and time-dependence of these diagonal peaks. The time-dependent fluctuations of the diagonal elements of the Hamiltonian, together with its static off-diagonal elements, lead to cross-relaxation between excitonic states that result in time-dependent cross-peaks in the 2D IR spectra. The simulated cross-peaks kinetics agree with those revealed from experiment extremely well and in a self-consistent manner as function of time as well as a function of surface concentration. In addition, the bi-exponential decay of the diagonal peaks is naturally explained by the excitonic model, while it had to be added in Ref. 13 in a purely phenomenological manner. Overall, the excitonic model can almost quantitatively reproduce the very rich set of experimental data with a fairly small set of parameters.

Population (T_1) relaxation very quickly masks the VET kinetics for lower **Re(CO)** concentrations. However, after having established the validity of the excitonic model, we could still study the mechanism of VET also on longer time by removing population relaxation in the simulations. For an isolated donor-acceptor dimer, the VET rate follows the expected $1/r^6$ dependence, similar to the NOE in NMR spectroscopy or FRET in electronic spectroscopy, with VET happening predominantly

between nearest neighbors. However, VET becomes a collective phenomenon on the surface, with the existence of a network of coupled **Re(CO)** molecules, and its disappearance below a percolation threshold, dominating the concentration dependence of the VET rate.

In an attempt to design an artificial photosynthetic system, we have recently studied electronic (Dexter-type) energy transfer between a similar Re(I) carbonyl complex co-adsorbed with a Co(I)-based catalyst for proton/water reduction on a metal oxide surface.[24] Just like here, we concluded that energy transfer is possible only between nearest neighbours. Whether the collective nature of energy migration, with a percolation threshold at a certain surface concentration, is also relevant for such artificial photosynthetic system,[24] we do not know at this point. One nice aspect about VET is the simplicity of the Hamiltonian, allowing one to study the process in great detail.

In conclusion, we believe that this work sets the stage for establishing VET in isotope-labelled molecules as a valuable tool to investigate, characterize and quantify the morphology of surface-bound catalysts, photosensitisers and mixtures of both. In addition, we believe the intermolecular distances and interactions can be studied by a careful analysis of the rich information contained in a 2D IR spectrum of such systems as a function of relative surface coverages. This, in turn, will serve to understand and elaborate on design criteria for functional and efficient light harvesting and artificial photosynthetic systems, where the intermolecular distances need to be optimally tuned to achieve better efficiencies and long-lasting performance.

Supplementary Material: Supplementary Material contains FTIR spectra to support the purity of the isotope-exchanged samples, as well as experiments determining the the surface coverage with **Re(CO)** and **CNBz** for the experiment described in Sec. VI.

Achnowledgement: We thank Dr. Laurent Sévery for the preparation of the TiO_2 films by ALD and spin-coating. Dr. Jan Philip Kraack and Dr. Jan Helbing are greatly acknowledged for insightful discussions. Dr. Angelo Frei and Prof. Dr. Roger Alberto are acknowledged for helpful discussions regarding the synthesis of the isotope-labelled complexes. We thank the Swiss National Science Foundation (Grant CRSII2_160801/1), and the University Research Priority Program (URPP) for Solar Light to Chemical Energy Conversion (LightChEC) of the University of Zurich for funding this research.

Availability of Data: Data available on request from the authors

Appendix A: Time Propagation Scheme

For the calculation of the time-evolution matrices needed to calculate 2D IR spectra, an approach different from Ref. 38 was used, which will be outlined in the following. As nicely discussed in Ref. 38, the time propagation of the two-exciton states is by far the most time-consuming part of the calculation of 2D IR spectra. Since the size of the two-exciton Hamiltonian is $N(N+1)/2$, while that of the one-exciton Hamiltonian is N (the number of coupled sites), and since any time-propagation scheme scales with a high power of the Hamiltonian size, the optimization of the overall performance of the algorithm needs to concentrate on the time-propagation of the two-exciton states.

We start by noting that one has two choices for the time propagation. That is, one may pre-calculate all the time-propagation matrices:

$$U(t_{k+1}, t_k) = \exp\left(-\frac{i}{\hbar} H(t_k)\Delta t\right), \tag{A1}$$

where $H(t_k)$ is the Hamiltonian matrix (which is assumed to be constant between t_k and t_{k+1}). With these time-propagation matrices, one may then propagate the wavefunction by calculating:

$$\Psi(t_{k+1}) = U(t_{k+1}, t_k)\Psi(t_k) \tag{A2}$$

Eq. A1 scales as N^3 for the one-exciton Hamiltonian, and N^6 for the two-exciton Hamiltonian for each time-propagation matrix. When one makes use of the sparseness of the two-exciton Hamiltonian,[36] the latter can be reduced to N^5. On the other hand, the computational cost of Eq. A2 scales as N^2 and N^4, respectively, with the smallest possible prefactor, i.e., a single matrix-vector product. Despite the fact that the two-exciton Hamiltonian matrix is sparse, the corresponding time-propagation matrix is not.

Alternatively, one may time-propagate the wave function directly with, e.g. the Chebyshev method.[50] This scales as N^2 for the one-exciton states, and N^4 (or N^3, when making use of the sparseness) for the two-exciton states, since the basic operation is a matrix-vector product as well. The prefactor, however, is larger; for the parameters of this work, approximately 20 Chebyshev iterations were needed, leading to ca. 20 matrix-vector products per time step.

There is a tradeoff between Eqs. A1 and A2 *versus* the Chebyshev propagation. That is, Eq. A1 has to be calculated only $n_1 + n_2 + n_3$ times, where n_1, n_2, and n_3 are the number of time-points along the t_1, t_2, and t_3 axes. On the contrary, Eqs. A2 and the Chebyshev propagation have to be calculated $n_1 \times n_2 \times n_3$ times for a complete 3D scan of the response function. For the one-exciton states, it turned out to be advantageous to use the method from Eqs. A1-A2, scaling as $N^3(n_1+n_2+n_3)$ and $N^2(n_1 \times n_2 \times n_3)$, respectively. For the two-exciton states, in contrast, the Chebyshev method turned out to

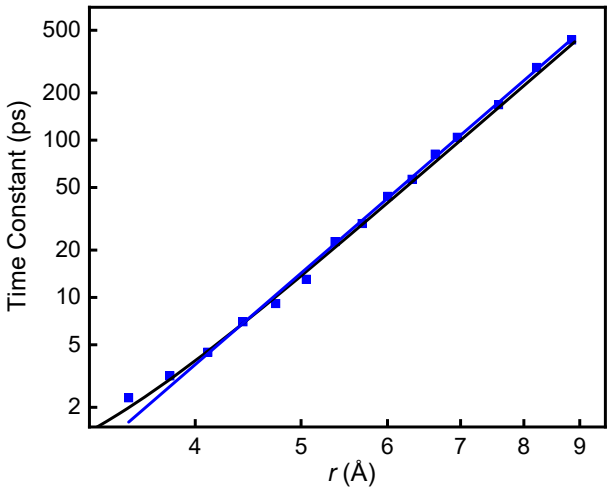

FIG. 10. Black line: VET rate according to Eq. 1 compared to the results from explicit time-propagation of the Hamiltonian (blue squares). The latter is fit to a r^6-dependence (blue line).

be significantly faster, scaling as $N^3(n_1 \times n_2 \times n_3)$, which is smaller than that of Eq. A1 (i.e., $N^5(n_1 + n_2 + n_3)$) despite the larger prefactor.

The overall scaling is therefore the same as in Ref. 38, where a Trotter expansion has been used instead of the Chebyshev method. The Trotter expansion, however, is approximate, and good only if the step size Δt is sufficiently small (values 10-20 fs have been used in Ref. 38). On the other hand, the Chebyshev method is numerically exact for any step size, with only a sub-linear dependence of the computational cost on step size.[50] We work here in a rotating frame with strong undersampling,[36] allowing us to use a step size of Δt=200 fs, which dramatically reduces the factor $n_1 \times n_2 \times n_3$ in comparison to Ref. 38. For a system with 50 coupled oscillators and a single realisation of the Hamiltonian, the calculation of a full set of 2D spectra with coherence times t_1 and t_3 ranging from 0-4 ps, and population times t_2 ranging from 0-40 ps, takes 36 s on the 4 cores of an Intel Xeon E5-2690 processor at 2.9 GHz (the algorithm can be easily parallelised). An average over typically 2000 such realisations is needed to achieve good signal-to-noise ratio, whose calculation takes ca. 20 h.

To compare Eq. 1 with the exciton model, we consider a dimer, and time-propagate it explicitly with the scheme introduced above. The following parameters were used to reveal a situation as simple as possible: Ω_{inhom} in Eq. 9 was set to zero and we consider only homogeneous dephasing with $T_2 = 0.5$ ps. The two transition dipoles ($\mu = 0.35$ D) were set parallel to each other and perpendicular to $\vec{r}_{DA}$. Fig. 10, shows in blue the VET rate as a function of intermolecular distance r, and compares it to Eq. 1 shown in black. Both agree extremely well when setting $\tau = \Delta t$, reflecting the fact that a new random set of diagonal elements has been assumed in the time-propagation of the Hamiltonian after each time-step Δt. For distances larger than ≈4.5 Å, the VET time constant follows the expected r^6 dependence, as indicated by the fit shown as blue line. The dependence is slightly less steep for shorter distances, where the dipole-dipole coupling V is no longer small compared to the energy splitting $\Delta\omega$ and/or the inverse of the dephasing correlation time τ^{-1} (see denominator of Eq. 1).

[1] R. Van Grondelle and V. I. Novoderezhkin, Phys. Chem. Chem. Phys. **8**, 793 (2006).
[2] L. Stryer and R. P. Haugland, Proc. Natl. Acad. Sci. U. S. A. **58**, 719 (1967).
[3] R. A. Bell and J. K. Saunders, Can. J. Chem. **48**, 1114 (1970).
[4] R. E. Schirmer, J. H. Noggle, J. P. Davis, and P. A. Hart, J. Am. Chem. Soc. **92**, 3266 (1970).
[5] H. Bian, H. Chen, J. Li, X. Wen, and J. Zheng, J. Phys. Chem. A **115**, 11657 (2011).
[6] H. Bian, X. Wen, J. Li, H. Chen, S. Han, X. Sun, J. Song, W. Zhuang, and J. Zheng, Proc. Natl. Acad. Sci. U. S. A. **108**, 4737 (2011).
[7] J. Li, H. Bian, X. Wen, H. Chen, K. Yuan, and J. Zheng, J. Phys. Chem. B **116**, 12284 (2012).
[8] H. Bian, J. Li, Q. Zhang, H. Chen, W. Zhuang, Y. Q. Gao, and J. Zheng, J. Phys. Chem. B **116**, 14426 (2012).
[9] J. Li, H. Bian, H. Chen, X. Wen, B. T. Hoang, and J. Zheng, J. Phys. Chem. B **117**, 4274 (2013).
[10] H. Chen, X. Wen, J. Li, and J. Zheng, J. Phys. Chem. A **118**, 2463 (2014).
[11] H. Chen, X. Wen, X. Guo, and J. Zheng, Phys. Chem. Chem. Phys. **16**, 13995 (2014).
[12] H. Chen, H. Bian, J. Li, X. Wen, Q. Zhang, W. Zhuang, and J. Zheng, J. Phys. Chem. B **119**, 4333 (2015).
[13] J. P. Kraack, A. Frei, R. Alberto, and P. Hamm, J. Phys. Chem. Lett. **8**, 2489 (2017).
[14] J. P. Kraack and P. Hamm, J. Phys. Chem. C **122**, 2259 (2018).
[15] J. P. Kraack, L. Sévery, S. D. Tilley, and P. Hamm, J. Phys. Chem. Lett. **9**, 49 (2018).
[16] S. Zhang, M. Li, W. Qiu, J. Han, H. Wang, and X. Liu, Appl. Catal. B Environ. **259**, 118113 (2019).
[17] C. D. Windle, E. Pastor, A. Reynal, A. C. Whitwood, Y. Vaynzof, J. R. Durrant, R. N. Perutz, and E. Reisner, Chem. - A Eur. J. **21**, 3746 (2015).
[18] M. Abdellah, A. M. El-Zohry, L. J. Antila, C. D. Windle, E. Reisner, and L. Hammarström, J. Am. Chem. Soc. **139**, 1226 (2017).
[19] J. Huang, M. G. Gatty, B. Xu, P. B. Pati, A. S. Etman, L. Tian, J. Sun, L. Hammarström, and H. Tian, Dalt. Trans. **47**, 10775 (2018).
[20] M. Waki, K. I. Yamanaka, S. Shirai, Y. Maegawa, Y. Goto, Y. Yamada, and S. Inagaki, Chem. - A Eur. J. **24**, 3846 (2018).
[21] L. Price, in *Energy Procedia*, Vol. 151 (Elsevier Ltd, 2018)

pp. 120–128.
[22] G. Sahara and O. Ishitani, Inorg. Chem. **54**, 5096 (2015).
[23] K. Oppelt, R. Fernández-Terán, R. Pfister, and P. Hamm, J. Phys. Chem. C **123**, 19952 (2019).
[24] K. Oppelt, M. Mosberger, J. Ruf, R. Fernández-Terán, B. Probst, R. Alberto, and P. Hamm, J. Phys. Chem. C **124**, 12502 (2020).
[25] N. Weder, B. Probst, L. Sévery, R. J. Fernández-Terán, J. Beckord, O. Blacque, S. D. Tilley, P. Hamm, J. Osterwalder, and R. Alberto, Catal. Sci. Technol. **10**, 2549 (2020).
[26] R. Alberto, A. Egli, U. Abram, K. Hegetschweiler, V. Gramlich, and P. A. Schubiger, J. Chem. Soc. Dalt. Trans. , 2815 (1994).
[27] J. M. Smieja and C. P. Kubiak, Inorg. Chem. **49**, 9283 (2010).
[28] J. P. Kraack, D. Lotti, and P. Hamm, J. Phys. Chem. Lett. **5**, 2325 (2014).
[29] P. Hamm, M. Lim, and R. M. Hochstrasser, J. Chem. Phys. **107**, 10523 (1997).
[30] P. Hamm, R. A. Kaindl, and J. Stenger, Opt. Lett. **25**, 1798 (2000).
[31] J. Helbing and P. Hamm, J. Opt. Soc. Am. B **28**, 171 (2011).
[32] R. Bloem, S. Garrett-Roe, H. Strzalka, P. Hamm, and P. Donaldson, Opt. Express **18**, 27067 (2010).
[33] K. Kwak, J. Zheng, H. Cang, and M. D. Fayer, J. Phys. Chem. B **110**, 19998 (2006).
[34] Q. Guo, P. Pagano, Y. L. Li, A. Kohen, and C. M. Cheatum, J. Chem. Phys. **142**, 212427 (2015).
[35] T. L. C. Jansen and J. Knoester, J. Phys. Chem. B **110**, 22910 (2006).
[36] P. Hamm and M. Zanni, *Concepts and methods of 2D infrared spectroscopy* (Cambridge University Press, Cambridge, 2011).
[37] N. G. Van Kampen, *Stochastic Processes in Physics and Chemistry* (Elsevier, Amsterdam, 1992).
[38] C. Liang and T. L. Jansen, J. Chem. Theory Comput. **8**, 1706 (2012).
[39] C. L. Anfuso, R. C. Snoeberger, A. M. Ricks, W. Liu, D. Xiao, V. S. Batista, and T. Lian, J. Am. Chem. Soc. **133**, 6922 (2011).
[40] C. L. Anfuso, D. Xiao, A. M. Ricks, C. F. Negre, V. S. Batista, and T. Lian, J. Phys. Chem. C **116**, 24107 (2012).
[41] A. Ge, B. Rudshteyn, B. T. Psciuk, D. Xiao, J. Song, C. L. Anfuso, A. M. Ricks, V. S. Batista, and T. Lian, J. Phys. Chem. C **120**, 20970 (2016).
[42] H. Vanselous, P. E. Videla, V. S. Batista, and P. B. Petersen, J. Phys. Chem. C **122**, 26018 (2018).
[43] M. Grechko and M. T. Zanni, J. Chem. Phys. **137**, 184202 (2012).
[44] C. L. Anfuso, A. M. Ricks, W. Rodríguez-Córdoba, and T. Lian, J. Phys. Chem. C **116**, 26377 (2012).
[45] J. Nishida, C. Yan, and M. D. Fayer, J. Chem. Phys. **146**, 094201 (2017).
[46] M. Delor, S. A. Archer, T. Keane, A. J. Meijer, I. V. Sazanovich, G. M. Greetham, M. Towrie, and J. A. Weinstein, Nat. Chem. **9**, 1099 (2017).
[47] D. E. Rosenfeld, Z. Gengeliczki, B. J. Smith, T. D. P. Stack, and M. D. Fayer, Science **334**, 634 (2011).
[48] T. Higashi and K. Osaki, Acta Crystallogr. Sect. B Struct. Crystallogr. Cryst. Chem. **37**, 777 (1981).
[49] M. Sahini and M. Sahimi, *Applications Of Percolation Theory* (CRC Press, Boca Raton, 1994).
[50] H. Tal-Ezer and R. Kosloff, J. Chem. Phys. **81**, 3967 (1984).